metals

MDPI

Article

The Influence of Manufacturing Parameters and Heat Treatments on the Properties of AlSi10Mg Alloy Produced Using L-PBF

Gleicy de Lima Xavier Ribeiro [1,2,*], Luis Reis [3,*], Rene de Oliveira [2], Marcos Massi [4], Rodolfo Luiz Gonçalves [4] and Antônio Augusto Couto [2,4]

[1] Senai Institute of Innovation in Advanced Manufacturing, 330 Vitória Maria Médice Ramos Street, São Bernardo do Campo 09861-790, SP, Brazil
[2] Institute of Energy and Nuclear Research, 2242 Professor Lineu Prestes Avenue, Butantã, São Paulo 05508-000, SP, Brazil
[3] IDMEC, Instituto Superior Técnico, Universidade de Lisboa, 1 Rovisco Pais Street, 1049-001 Lisboa, Portugal
[4] Engeneering School, Mackenzie Presbyterian University, 930 Consolação Street, Consolação, São Paulo 01302-907, SP, Brazil
* Correspondence: gleicy.limaxavier@gmail.com (G.d.L.X.R.); luis.g.reis@tecnico.ulisboa.pt (L.R.)

Abstract

AlSi10Mg has been one of the most studied and employed aluminum alloys for additive manufacturing via laser powder-bed fusion (L-PBF). The optimization of manufacturing parameters is important for reducing internal defects, including porosity and inadequate surface finishes. In addition, heat treatments, such as T6, are often applied to this alloy, but they degrade the characteristic microstructure obtained via L-PBF additive manufacturing—the fine cellular structures—which may, in turn, detrimentally affect the material's properties. In this context, a new alternative to this treatment, direct aging (DA), has shown promise in improving the mechanical properties of AlSi10Mg parts produced via L-PBF, since it preserves the cellular microstructure, precipitating silicon-rich nanoparticles within the cells. Understanding how different temperatures and heat treatment times influence the microstructure and, consequently, the properties remains a field to be explored in order to optimize the treatment conditions and achieve better mechanical properties. Thus, the objective of this study was to evaluate the influence of manufacturing parameters and heat treatments on the microstructure and mechanical properties of AlSi10Mg alloy. The optimized manufacturing conditions were 300 W power, 800 mm/s scan speed, 30 µm layer thickness, and an argon atmosphere, which led to lower porosity and better finishing. Samples were heat-treated via DA at 150 °C and 170 °C for different times, as well as undergoing a T6 treatment (solution at 520 °C followed by aging at 150 °C and 170 °C). Initially, the aging curves show higher hardness values for the direct aging condition, compared to the T6 and as-built conditions, reaching a peak hardness of 195 HV for 6h of direct aging. In this way, it was followed with microstructural characterization, which demonstrated that DA maintained the fine cell microstructure of L-PBF and promoted the precipitation of Si nanoparticles, which certainly contributed to the increase in hardness compared to T6, which promoted a structure with coarser precipitates. DA at 170 °C for 6 h increased the tensile strength to 430 MPa, compared to the as-built condition, with a slight loss of ductility.

Keywords: heat treatment; direct aging; additive manufacturing; AlSi10Mg; L-PBF

Academic Editors: Chonghe Li and Qisheng Feng

Received: 24 July 2025
Revised: 15 August 2025
Accepted: 21 August 2025
Published: 25 August 2025

Citation: Ribeiro, G.d.L.X.; Reis, L.; de Oliveira, R.; Massi, M.; Gonçalves, R.L.; Couto, A.A. The Influence of Manufacturing Parameters and Heat Treatments on the Properties of AlSi10Mg Alloy Produced Using L-PBF. *Metals* **2025**, *15*, 941. https://doi.org/10.3390/met15090941

1. Introduction

The need for manufacturing processes to obtain parts with complex and customized geometries that optimize weight, save material, and reduce items in assembly, among other demands, has stimulated the diffusion of additive manufacturing. The process that stands out the most in the production of metal parts and high-performance structural components is laser powder-bed fusion (L-PBF). This technology consists of manufacturing components by adding material layer by layer using information obtained from a 3D computational geometric representation [1].

Interest in the additive manufacturing (AM) of aluminum alloys continues to increase, due to the possible recycling of this material, its high strength-to-weight ratio, and its thermal and electrical conductivity properties [2]. AlSi10Mg alloy is the most used alloy in the powder-bed fusion process due to its good weldability and high melting fluidity. However, the use of this material is still limited compared to other alloys because specific challenges still hinder the 3D printing process. The low absorption of laser radiation by this aluminum alloy remains a challenge at commonly used wavelengths, requiring high energies to promote fusion, which can result in the evaporation of alloying elements [3]. Furthermore, balancing the combination of process parameters to prevent defect formation, while considering the risks of overheating due to the high reflectivity of aluminum, must be carefully optimized and consolidated. This balance is essential to achieve components with minimal defects and improved mechanical properties, without compromising the safe operation of the process [4–6]. In addition to the careful control of manufacturing parameters, heat treatments must also be thoroughly evaluated, as they can directly influence the mechanical properties. Certain heat treatments like T6 may degrade the characteristic cellular microstructure achieved with additive manufacturing, leading to the formation of coarse precipitates that can compromise the mechanical strength of the produced parts, while some can preserve the characteristic microstructure [5,7–10].

Different fusion regimes—conduction, transition, and keyholing—can occur due to the combination of processing parameters, even when the input energy density remains constant. These regimes directly affect the microstructure, the distribution of residual stresses, and, consequently, the mechanical properties and the final quality of the part [11]. Although increasing energy density may reduce surface roughness, turbulences associated with the keyhole regime often result in the formation of significant internal porosities, which may compromise mechanical properties, especially fatigue resistance. Thus, there is a trade-off between surface roughness, hardness, and structural integrity, resulting from the processing conditions adopted [12,13].

Keyhole porosity can arise when fusion occurs at very high power densities in keyhole mode without proper control. In these situations, the keyhole can become unstable and collapse, leaving almost spherical-shaped voids with trapped gas [14]. This porosity can vary in size and shape depending on the geometry and stability of the keyhole. Gas-trapping pores are typically microscopic (between 5 and 20 μm), have a perfectly spherical shape, and may originate from the gases trapped inside the powder particles in the atomization step. On the other hand, defects due to a lack of fusion are associated with inadequate penetration of the melt pool into the already deposited layer or building base. This type of defect tends to have a more irregular and elongated shape, indicating insufficient input energy [15]. Surface roughness is also strongly influenced by several factors, such as the design of the part, the characteristics of the powder, the scanning strategy, and the process parameters. The two main causes of surface roughness are the stair-step effect and the balling effect. The first occurs on curved or inclined surfaces, due to the staggered approximation of the layers, their intensity dependent on the layer thickness, and the construction angle. The balling effect is related to instabilities in the melt pool, especially at

high scanning speeds, causing the molten metal to fragment into small, solidified spheres, which often accumulate at the edges of the laser tracks, increasing roughness. Another possible cause of roughness is the presence of unfused particles, which can be ejected out of the part when the energy supply is insufficient to promote complete fusion of the powder [12,15].

Volumetric Energy Density (VED) is a parameter that can directly influence the quality of parts produced by LPB-F. It is determined by the ratio between laser power, scanning speed, and powder bed geometry, such as layer thickness and the distance between laser tracks (hatch distance). It is a way to correlate these parameters, and an inadequate adjustment of energy density can cause defects such as porosity due to lack of fusion or excessive evaporation of the material. Studies indicate that optimizing VED-related parameters allows us to produce continuous layers with higher density, ensuring the desired structural integrity and mechanical properties. VED can be calculated according to Equation (1) [16,17], where P is the power, V é the scanning speed, H is the hatch space, and T is the layer thickness.

$$\text{VED} = \frac{P}{V * H * T} \tag{1}$$

Thus, optimization of process parameters is fundamental for manufacturing parts with adequate mechanical properties to reduce defects inherent in the powder-bed fusion technique [3,18–20].

Generally, alloys manufactured via additive manufacturing require post-processing, either for the surface finishing of the parts or for improving their functional properties. Heat treatments are important in prepossessing, as they can relieve residual stresses generated by successive heating, melting, and cooling cycles, as well as promote microstructural modifications to help improve mechanical properties. For thermally treatable aluminum alloys, one of the most used treatments is T6, which consists of a solution step at elevated temperatures, between 500 °C and 570 °C, followed by rapid cooling (usually in water) and subsequent artificial aging, between 120 °C and 180 °C. However, an alternative that has been gaining prominence in the literature is direct aging, which dispenses with the solution step and seeks to optimize mechanical properties through a simpler and more energy-efficient thermal process, with aging temperatures between 120 °C and 180 °C [21–25].

The L-PBF process involves high solidification rates (1–2 m/s), thus promoting rapid cooling outside of thermodynamic equilibrium. At the nanoscale, this accelerated cooling increases the solubility limit of silicon in aluminum from 1.62% wt to values between 2.8% and 3.6% [8]. As a result, the parts produced in the as-built state exhibit a fine cellular microstructure, composed of a eutectic silicon network surrounding a supersaturated α-Al matrix. When subjected to T6 heat treatment, parts manufactured by L-PBF undergo significant transformations. The solution step, performed at high temperatures, promotes dissolution of the eutectic silicon network, while subsequent aging induces precipitation of particles from the supersaturated solid solution. These precipitates become reinforcement mechanisms for the metal matrix, helping to harden the alloy [25].

Thus, direct aging heat treatment preserves the cellular structures formed during solidification while maintaining the eutectic silicon networks around the α-Al matrix. This treatment promotes precipitation of silicon-rich nanoparticles within α-Al cells, reinforcing the matrix without degrading the microstructure characteristic of the additive manufacturing. According to Egidio et al. [23], precipitation starts from the supersaturated solid solution α(SSS), and the precipitation of the reinforcement phases during aging follows a specific path, as described in Equation (2). Therefore, the analysis aims to better understand how to optimize aging conditions to strengthen the alloy.

$$\alpha(\text{SSS}) \rightarrow \text{GP zones} \rightarrow \beta'' \rightarrow \beta' \rightarrow \beta \tag{2}$$

GP zones (Guinier–Preston zones) or "pre-precipitation zones" refer to structures that form in aluminum alloys with added magnesium, such as AlSi10Mg, during the aging process. These zones are composed of small clusters of atoms, often enriched in silicon, which become stable and play an essential role in hardening the alloy. The formation of GP zones is a critical precursor for the precipitation of more stable phases, such as Mg_2Si, which promote increased mechanical strength of the alloy throughout the heat treatment. Thus, the presence and development of the GP zones significantly impact the mechanical properties and aging of the aluminum alloys. As the intensity of the thermal exposure increases—either by raising the temperature or extending the aging time—the hardening precipitates coalesce, evolving through intermediate forms, such as the β'' and β' phases, until they reach the incoherent stable phase β. These larger precipitates contribute less to alloy hardening due to the following: (i) smaller interface area between the precipitates and the matrix, (ii) greater incoherence between the hardening phases and the α-Al matrix, and (iii) lower density of dispersed particles.

Thus, the combination of the optimization of manufacturing parameters—focused on reducing internal defects and applying suitable heat treatment conditions—and the choice of suitable heat treatment conditions is an effective strategy to improve the mechanical properties of parts produced by L-PBF. The present work aims to improve the manufacturing parameters of the AlSi10Mg alloy, aiming to minimize porosity, as well as study the effects of T6 heat treatment and direct aging on the mechanical properties of the material.

2. Materials and Methods

2.1. Optimization of Manufacturing Parameters

The feedstock used in the fusion process on a laser powder bed was AlSi10Mg alloy (LaserForm Aluminum, 3D Systems, Rock Hill, SC, USA), gas atomized, with composition according to the supplier, as provided in Table 1. Scanning electron microscopy (TM3000, Hitachi, Tokyo, Japan) was performed to evaluate the morphology of the particles, and the determination of the specific mass was made using helium gas pycnometry. The initial material was also subjected to the low-temperature drying process (4 h at 60 °C) to improve its flowability.

Table 1. Chemical composition of AlSi10Mg powder for laser powder-bed fusion.

Element	Si	Fe	Cu	Zn	Mn	Ti	Mg	O	Al
% by wt	9.9	0.12	<0.01	0.02	<0.01	<0.01	0.35	0.05	balance

Laser powder-bed fusion was conducted in an argon atmosphere, with an ytterbium fiber laser, with a wavelength of 1070 nm (OmniSint-160®, Ommitek Technology, Campinas, Brazil). The laser beam scanning shifted or rotated the angle by 67° for each layer. Cubic samples of 10 × 10 × 10 mm were produced, as shown in Figure 1.

To optimize the manufacturing process, the hatch space parameter was optimized in Step 1, while Step 2 entailed optimization of the laser power and scan speed parameters.

In Step 1, the power parameters (250 W), scanning speed (1000 mm/s), layer thickness (30 µm), beam diameter (90 µm), and 0° orientation in relation to the construction base were kept constant. The hatch space was varied to 70, 80, and 100 µm, conditions C1, C2, and C3, respectively.

In Step 2, the hatch space (defined as the best condition from Step 1), layer thickness (30 µm), beam diameter (90 µm), and 0° orientation in relation to the construction base remained fixed, while varying the power from 200 to 300 W and the scanning speed from

800 to 1200 mm/s, obtaining a matrix with nine power-speed combinations, with samples named from A to I.

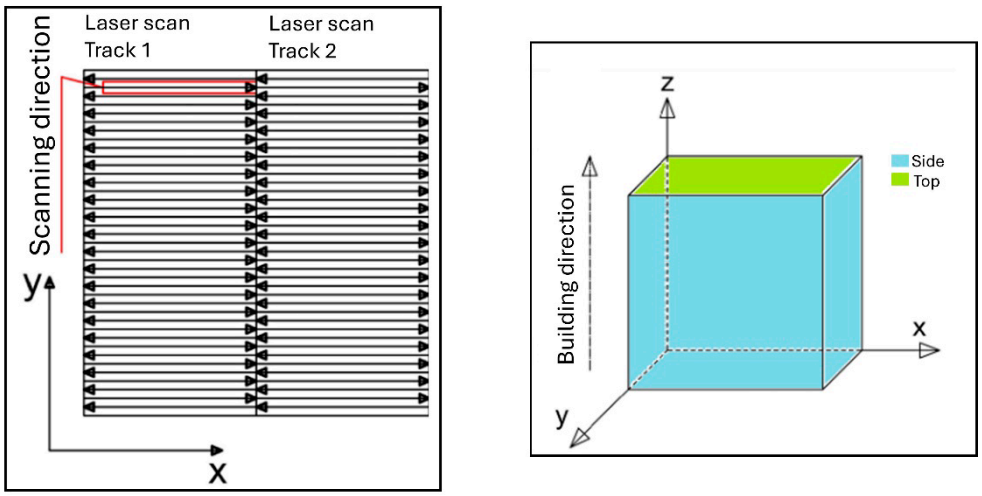

(**a**) (**b**)

Figure 1. (**a**) Laser scanning strategy in the layers and (**b**) building direction and top and side sections.

For all steps, the VED (Volumetric Energy Density) was calculated to all combination parameters, according to Equation (1) [16].

The samples from Steps 1 and 2 were characterized by industrial X-ray tomography (Metrotom 800, Carl Zeiss, Oberkochen, Germany) to evaluate 3D porosity. Was evaluated percentage of pore volume, distribution of the diameters, and the pore sphericity. Table 2 provides samples scanning parameters. The evaluations were performed using the VGStudio max 2022.1 software and the algorithm used was the "only threshold". As the detection limit, the voxel size (20 µm) was considered.

Table 2. X-ray tomography scan parameters of the samples produced via LPB-F in Steps 1 and 2.

Voltage: 100 kV	Current: 140 µA
Spot size: 20 µm	Voxel size: 20 µm
Detector: (1456 × 1840) px	Number of projections: 1000
Integration time/Gain: 1000 ms/2.5x	Prefilter: -

The samples from Step 2 were evaluated for their 3D roughness using light interferometry (Zagueage, Zygo, Middlefield, OH, USA) in an area of 1.4 × 1.4 mm, obtaining the average roughness parameters in area (Sa). For both steps, the criterion to define the best parameter was, first, the lowest porosity found, and second, the least roughness. After determining the best hatch space condition and the best combination of power and speed, cubic samples and rectangular bars were manufactured to fabricate the tensile specimens.

2.2. Heat Treatment

The cubic samples, manufactured in the optimized condition, were subjected to two types of heat treatment. The T6 consisted of solution at 520 °C for 2 h, followed by cooling in water at room temperature, and subsequent aging at different times with air cooling. The direct aging was also performed at different times with air cooling. Figure 2 presents a schematic flowchart of the heat treatment conditions employed. The solution treatment was carried out in a muffle furnace with heating capacity up to 600 °C, and the aging and direct aging treatments were conducted in an oven with heating capacity up to 250 °C.

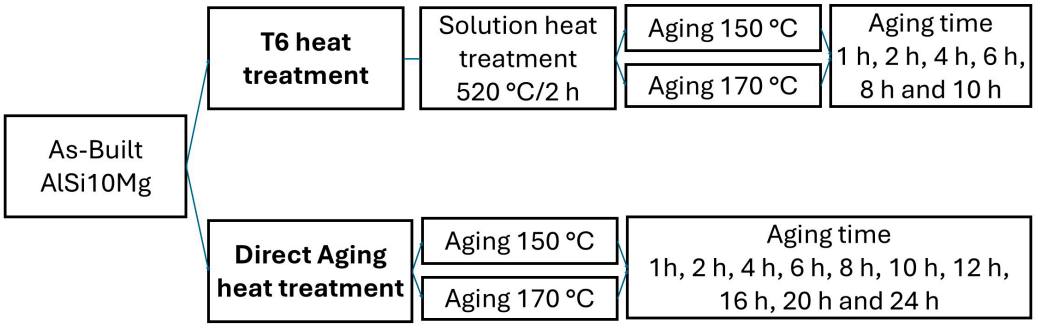

Figure 2. Schematic flowchart of the heat treatment conditions.

Microhardness on the Vickers scale was measured on an automatic microdurometer (Duramin-40 AC3, Struers, Copenhagen, Denmark). The treated and as-built samples were cut in the ZY plane, using a precision cutter with diamond disk (IsoMet, Buehler, Lake Bluff, USA), hot-embedded with Bakelite, and sanded with SiC sandpaper until 600 grits. Indentations were made in building direction, in two lines with five points each, calculating the average, disregarding the highest and lowest value found among the ten points, as well as calculating the standard deviation.

X-ray diffraction analyses (Multiflex, Rigaku, Tokyo, Japan) to identify the phases present were performed using Cu-Kα (λ = 1.5418 Å), with a voltage of 40 kV and a current of 20 mA. The angular range 2θ adopted was 20° to 90°, with a scanning speed of 2° per min.

For the microstructural analysis, the treated and as-built samples were prepared according to metallographic standards in an automatic preparation machine (X-Matic, Struers, Copenhagen, Denmark) and attacked with Keller reagent for 30 s to reveal the microstructure. Samples were analyzed at different magnifications by field emission scanning electron microscopy (JSM-IT700HR, JEOL, Tokyo, Japan).

2.3. Mechanical Tests

The tensile specimens were subjected to direct aging at 150 and 170 °C for 6 h and 10 h. The mechanical tests were performed on the heat-treated specimens and the as-built condition, using a 50 kN universal testing machine (Criterion 40, MTS, Eden Prairie, MN, USA), with a displacement speed of 0.195 mm/min and at room temperature. At least three specimens of each condition were tested, and the stress–strain curves were obtained. The properties were calculated based on the average of the three values.

3. Results and Discussion

3.1. Feedstock Characterization

Figure 3 shows the image obtained by SEM with backscattered electrons of the gas atomized powder of the AlSi10Mg alloy. The particles are predominantly spherical in shape, with the presence of satellite particles (smaller particles coupled to larger ones) and a few more elongated particles. This varied composition of sizes and shapes is characteristic of the gas atomization process and is important for filling in the voids between the larger powder grains to improve the fusion process. The specific mass of the powder, determined using helium gas pycnometry, was 2.65 g.cm^{-3}.

During particle size analysis performed by the supplier, in accordance with ASTM B214, the fraction of particles with diameters greater than 63 µm was evaluated, establishing a maximum limit of 5 wt%. The results showed the presence of this fraction only at trace levels, below the quantification limit of the method.

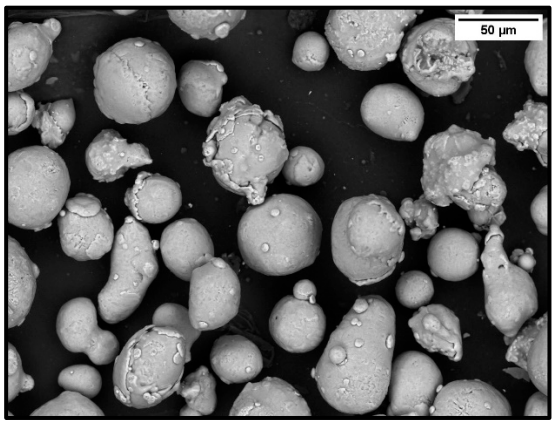

Figure 3. Scanning electron microscopy of gas-atomized AlSi10Mg alloy powder.

3.2. Optimization of Manufacturing Parameters

For Step 1, moderate power and a higher scanning speed were selected to evaluate the performance of the equipment and the manufacturing process with the combinations of these parameters. This choice took into consideration that aluminum alloys have high reflectivity at wavelengths in the infrared range (1070 nm), and very high power associated with slow speeds could cause overheating that damages the equipment. This choice was also based on the literature [26].

Figure 4a–c shows the distribution graphs of the pore diameters identified in samples C1, C2, and C3, respectively, obtained in Step 1, while (d) is the graph of the volumetric energy density for the total number of defects and the volumetric percentage of defects in the samples.

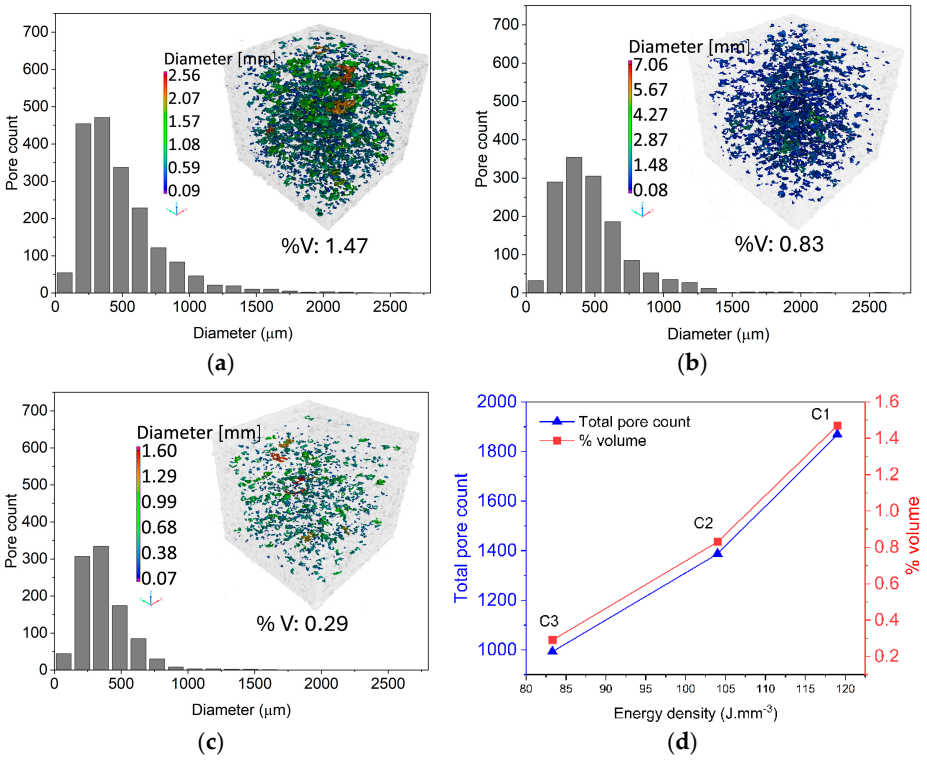

Figure 4. Three-dimensional porosity and distribution chart of pore diameters in the Step 1 samples. Laser scanning speed of 1000 mm/s, power of 250 W, (**a**) C1—70 µm hatch space, (**b**) C2—80 µm hatch space, and (**c**) C3—100 µm hatch space. (**d**) Relationship between the volumetric energy density, the quantity of pores, and the volumetric percentage of pores.

The distribution graphs of pore diameters illustrate that samples C1, C2, and C3, produced with hatch spaces of 70 µm, 80 µm, and 100 µm, respectively, have asymmetric distributions, concentrating pores up to approximately 500 µm. Sample C1 (70 µm) exhibited the highest total pore quantity (1868), the highest volumetric porosity (1.47%), and the broadest distribution. Sample C3 (100 µm) had the lowest total number of pores (993) and the lowest volumetric porosity (0.29%), with a significant pore concentration between 100 and 300 µm, indicating that smaller pores predominated.

The hatch space directly influences the energy density delivered to the material. Larger hatch space reduces energy density but can generate unfused regions between laser passes, and thus porosity. However, a very narrow hatch space promotes excessive overlap and heat buildup, making fusion unstable. In sample C1, the combination of high overlap and excessive heat may have induced the keyhole effect, characterized by deep melting pools, material evaporation, and gas trapping.

The volumetric energy density (VED) should be sufficiently high to ensure complete particle fusion and good layer coalescence. Insufficient VED results in partial fusion and increased porosity. Furthermore, variations in the geometry of the melt pool directly affect the final porosity, i.e., small or irregular melt pools that solidify in a non-uniform manner often form voids. An aspect ratio value of the melt pool near 0.4 is cited as optimal for stability in the process; melt pools with greater depth than width increase the risk of defects due to the higher incidence of trapped vapors [27]. Furthermore, the cooling and solidification rates, also modulated by VED, directly impact pore formation [11]. Thus, Step 1 elucidated that 100 µm was the best hatch space condition, causing the lowest porosity indexes.

Table 3 presents the 3D porosity values, with the pore volume percentage for samples A to I, of the parameter matrix obtained in Step 2, in which different laser scanning powers and speeds were used.

Table 3. Percent by volume of pores found in samples A to I produced in Step 2.

		Scan Speed (mm/s)		
		800	1000	1200
		Percent by volume of pores		
Power (W)	200	A (1.08)	B (2.97)	C (3.80)
	250	D (1.29)	E (0.42)	F (0.40)
	300	G (0.23)	H (0.25)	I (0.43)

Figures 5–7 illustrates the 3D porosities of the Samples A to I of the parameter matrix obtained in Step 2, in which different laser scanning powers and speeds were used.

The variation in the scanning speed and laser power parameters in Step 2 demonstrated that at lower powers, the 3D porosity (%volume) increased significantly as the speed increased. At higher speeds, the interaction time of the laser with the material decreases, reducing the effective melting of the powder. This resulted in an incomplete fusion, forming pores and irregularities at the interface between layers [15]. This effect is evident in the porosity values, which increase from 1.08% at 800 mm/s to 3.80% at 1200 mm/s, demonstrating that higher speeds, when not accompanied by a proportional increase in power, result in poor fusion.

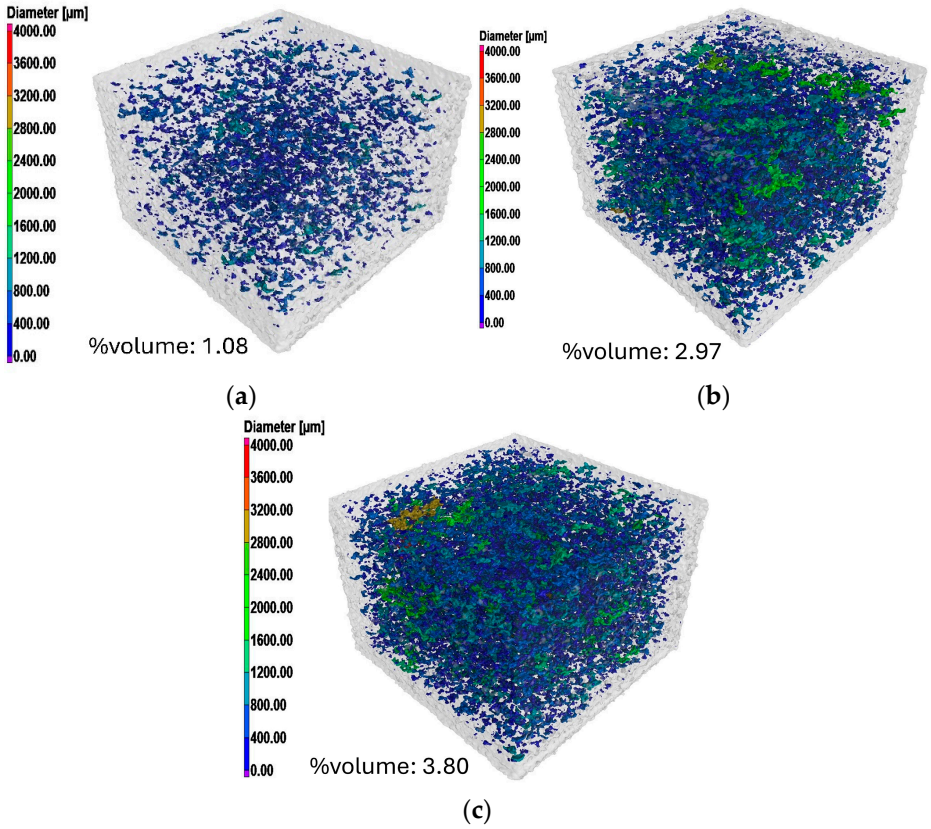

Figure 5. Three-dimensional porosity (%volume) of the samples from Step 2 to 200 W power and (**a**) Sample A—800 mm/s; (**b**) Sample B—1000 mm/s; (**c**) Sample C—1200 mm/s.

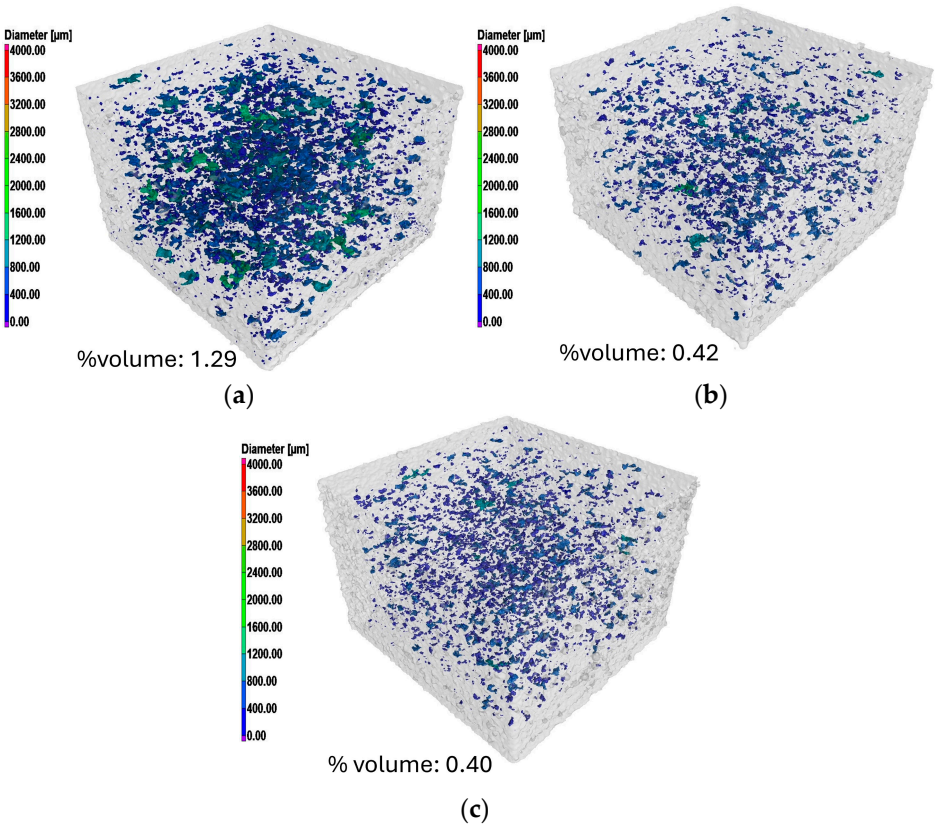

Figure 6. Three-dimensional porosity (%volume) of the samples from Step 2 to 250 W power and (**a**) Sample D—800 mm/s; (**b**) Sample E—1000 mm/s; (**c**) Sample F—1200 mm/s.

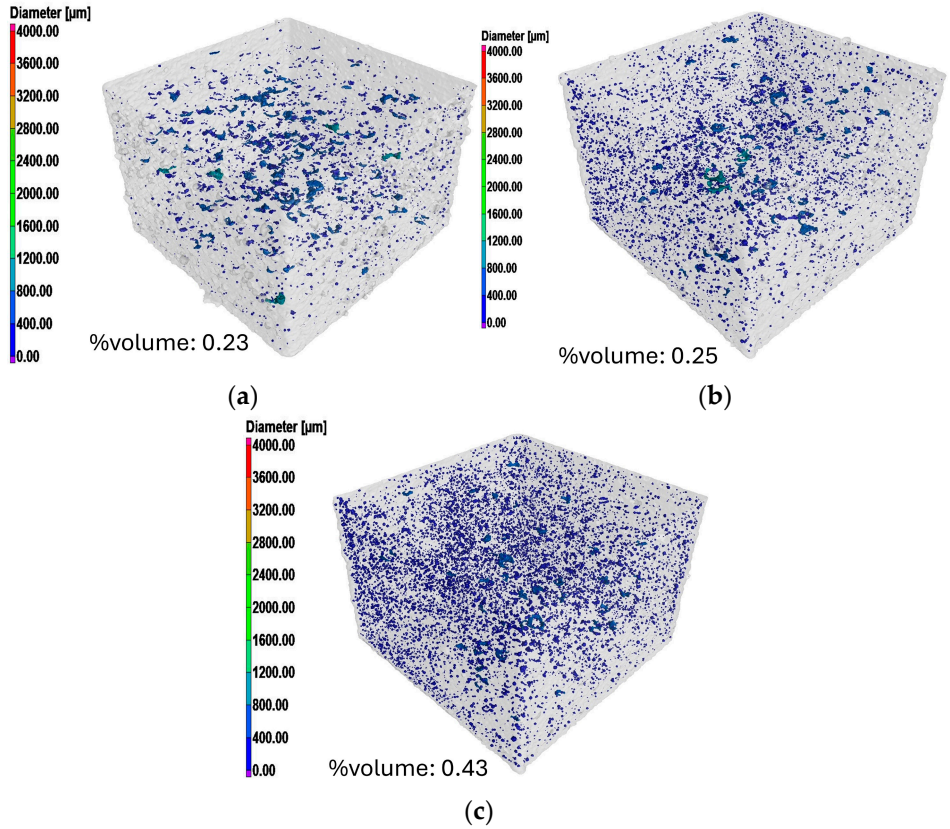

Figure 7. Three-dimensional porosity (%volume) of the samples from Step 2 to 300 W power and (**a**) Sample G—800 mm/s; (**b**) Sample H—1000 mm/s; (**c**) Sample I—1200 mm/s.

However, when the laser power increases to 250 W, the porosity significantly reduced. The values drop to 0.42% and 0.40% at intermediate and high speeds, suggesting that the higher energy availability was sufficient to promote complete fusion, avoiding pores and incomplete fusion. This behavior was already reported by Yadroitsev et al. [28], indicating that the stability of the melt pool improves as the energy supplied increases, reducing the presence of porosity due to a lack of fusion.

With 300 W of power, the porosity reaches the lowest values, below 0.43% for all speeds used, indicating that an increase in energy input is one of the most efficient ways to reduce defects. This corroborates studies [29] that found that increased energy density helps eliminate incomplete fusion pores and reduce the presence of voids between the layers.

Figure 8 shows the relationship between energy density, the total number of pores, and the volumetric percentage of pores.

Figure 9 presents the distribution graphs of the pore diameters of samples A to I, produced in Step 2.

Analyzing the distribution of pore diameters in samples A to I, most pores have diameters below 200 µm, regardless of the condition employed. Samples with lower VED—such as C (200 W and 1200 mm/s; VED = 55.56 J/mm^3), F (250 W and 1200 mm/s; VED = 69.44 J/mm^3) and I (300 W and 1200 mm/s; VED = 83.33 J/mm^3)—exhibited a higher total number of pores within their respective power groups. The high quantity of pores and the high volumetric porosity of sample C, for example, may suggest that the energy was insufficient to completely melt the metallic powder, as the high laser scanning speeds decrease the interaction time of the beam with the material, which favors incomplete fusion, poor cohesion between the layers, and the formation of pores due to lack of melting [30,31]. As the VED increases, either by higher power or lower speed, the total number of pores and the volumetric porosity are reduced. Samples such as G (300 W

and 800 mm/s; VED = 125 J/mm^3), D (250 W and 800 mm/s; VED = 104.17 J/mm^3), and A (200 W and 800 mm/s; VED = 83.33 J/mm^3) exhibit lower porosities (~0.2 to 1.3%) and reduce the number of pores. However, this relationship is not always linear. For example, samples F and I, with intermediate VEDs and similar volumetric porosity, exhibit a different total quantity of pores (5173 and 13,461, respectively), with sample I being characterized by smaller pores, possibly due to instability in fusion and gas trapping. In addition, the lower the energy density, the greater the dispersion in diameters, creating larger pores. However, at high VEDs, the distribution tends to be concentrated in smaller diameters (<200 µm), consistent with more stable and homogeneous fusion regimes, creating predominance of spherical pores due to gas trapping [32].

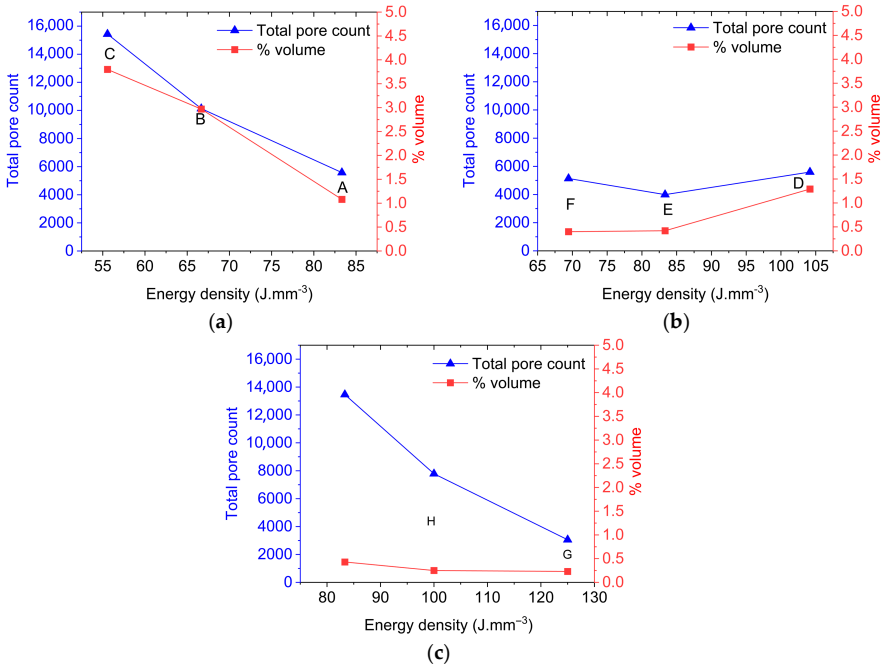

Figure 8. Graph of volumetric density related to the volumetric percentage of pores and the total number of pores to samples from Step 2. (**a**) Samples A, B and C. (**b**) Samples D, E and F. (**c**) Samples G, H and I.

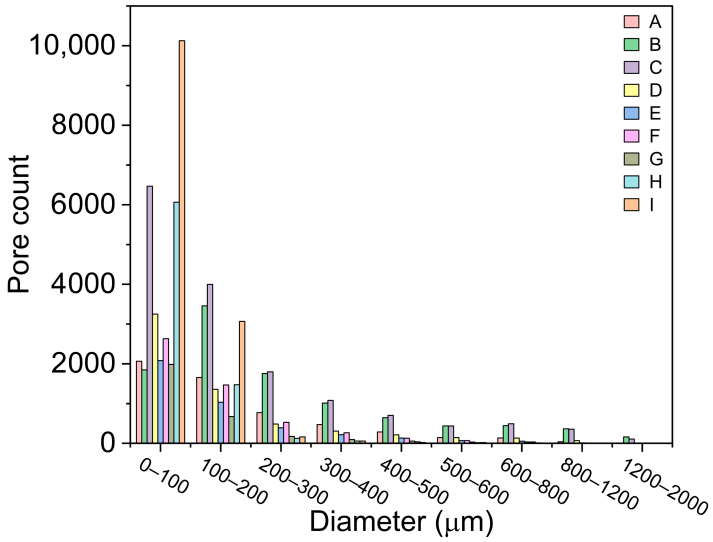

Figure 9. Distribution graph of pore diameters found in samples A to I from Step 2. Sample A, B and C: 200 W power, 800 mm/s, 1000 mm/s and 1200 mm/s, respectively. Sample D, E and F: 250 W power, 800 mm/s, 1000 mm/s and 1200 mm/s, respectively. Sample G, H and I: 300 W power, 800 mm/s, 1000 mm/s and 1200 mm/s, respectively.

Figure 10 presents the graphs of sphericity distribution of the pores in samples A to I, produced in Step 2.

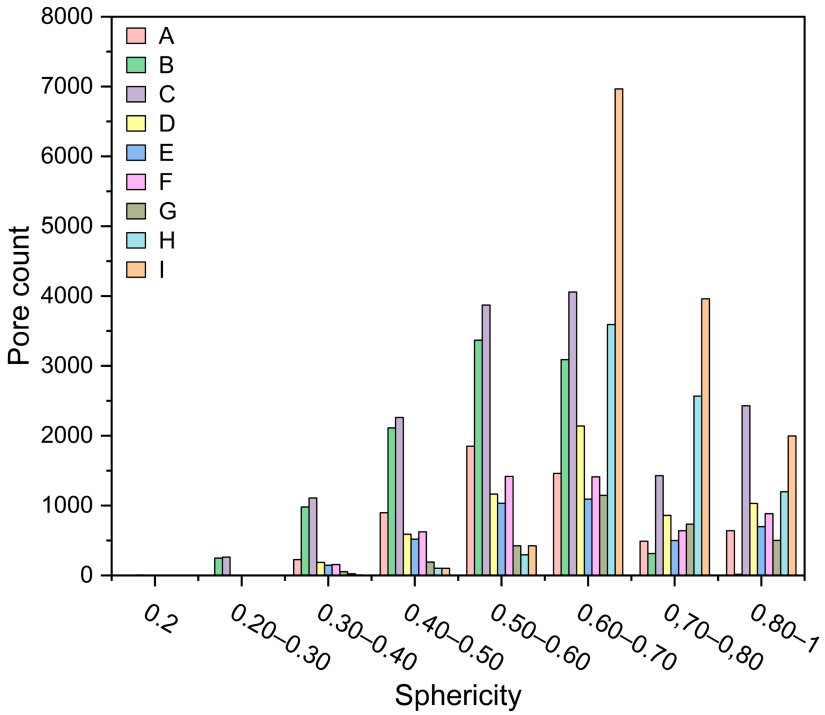

Figure 10. Distribution of pore sphericity in samples A to I from Step 2. Sample A, B and C: 200 W power, 800 mm/s, 1000 mm/s and 1200 mm/s, respectively. Sample D, E and F: 250 W power, 800 mm/s, 1000 mm/s and 1200 mm/s, respectively. Sample G, H and I: 300 W power, 800 mm/s, 1000 mm/s and 1200 mm/s, respectively.

The sphericity of the pores indicates the mechanism of their formation, i.e., the more spherical pores are usually characteristic of gas trapping, while the irregular ones are caused by the lack of fusion and instabilities in the melt pool [33]. In samples with higher energy density, as in the case of sample G (300 W and 800 mm/s; VED = 125 J/mm^3), the sphericity is concentrated between 0.6 and 0.9, suggesting that the more stable, homogeneous, and efficient fusion eliminated gases. On the other hand, samples with low VED, such as C (200 W and 1200 mm/s; VED = 55.56 J/mm^3), exhibit greater dispersion in sphericity, with a greater occurrence of pores between 0.3 and 0.6, characterizing elongated and irregular pores, which are usually due to a lack of fusion [17]. In addition, increasing the scanning speed and keeping the power constant reduced the average sphericity of the pores, as observed in samples A, B, and C. This behavior is related to more intense thermal gradients and abrupt cooling. Intermediate VEDs, as in samples E and F, create a more homogeneous sphericity distribution, indicating a transition between gas formation mechanisms and lack of fusion.

Table 4 lists the mean roughness values Sa of the samples produced in Step 2, from the lateral (ZY plane) and top (XY plane) planes.

Comparing the Sa values of the samples produced in Step 2 elucidates significant differences between the lateral (ZY) and top (XY) planes, directly influenced by the processing parameters, including laser power and scanning speed. The roughness in the lateral plane tends to be higher than in the top plane, reflecting the formation of the layers in the L-PBF process. The successive overlap of the fusion tracks generates irregularities due to non-uniform solidification, thermal instabilities, and the “step effect”, characteristic of this type of manufacturing. As already mentioned, this characteristic occurs because the lateral

surface suffers from the stacking of the layers, while the top plane benefits from a more stable thermal profile and direct contact with the powder [28].

Table 4. Mean roughness parameter values in Sa area (μm) for the lateral (ZY) and top (XY) planes of the samples obtained in Step 2.

		Scan Speed (mm/s)					
		800		1000		1200	
		Roughness (Sa Parameter)					
Plane		ZY	XY	ZY	XY	ZY	XY
Power (W)	200	32.52	11.57	32.59	30.30	27.34	21.18
	250	23.75	17.62	24.57	15.98	27.98	16.72
	300	22.74	10.62	23.90	18.38	11.25	7.7

When analyzing the influence of laser power, increasing the power reduces surface roughness. Thus, higher powers improve the fusion of the material, resulting in more homogeneous deposition and minimizing defects, including porosity and incomplete fusion. This behavior is evident in the lateral plane, where roughness decreases from 32.52 μm (200 W and 800 mm/s) to 11.25 μm (300 W and 1200 mm/s). Some studies corroborate this trend, pointing out that the use of greater power improves the wettability of the melt pool, reducing superficial irregularities [34].

The obtained values demonstrate that the roughness tends to decrease with increasing speed, especially in combinations with power of 300 W. This phenomenon occurs because higher speeds reduce the interaction time of the laser with the material, avoiding excessive fusion and decreasing the formation of solidified droplets (balling effect), which impair the quality of the surface. However, excessively high speeds can lead to incomplete fusion, causing the opposite effect, as noted in the lateral plane of the 250 W combinations.

Therefore, higher scanning speeds and powers tend to produce a better surface finish, especially in the combination of 300 W and 1200 mm/s. This agrees with previous studies on L-PBF, which demonstrated that the combination of greater power and optimized speed favors the fluidity of the melt pool, reducing surface defects and providing a more uniform texture [29].

Thus according to the results presented, which sought to evaluate the influence of the manufacturing parameters on porosity, related to volumetric porosity, pore sphericity, and pore diameter, as well as on the surface finish, the manufacturing condition of sample G, in which laser power of 300 W and scanning speed of 800 mm/s was used, along with layer thickness of 30 μm, beam diameter of 90 μm, argon atmosphere, and hatch space of 100 μm, was the best combination in this work.

3.3. Heat Treatment

Figure 11 presents the aging curves of the AlSi10Mg alloy subjected to T6 treatment and direct aging, with temperatures of 150 °C and 170 °C, applied for different times. All heat-treated samples were manufactured using the optimized additive manufacturing

The sample in as-built state presented a hardness value of 169 HV. Similar harness value for as-built samples was reported by Fernandes et al. [35]. Egidio et al. [23] and Zheng et al. [36] obtained lower hardness values for as-built samples; however, the manufacturing parameters were considerably different, resulting in distinct heating and cooling cycles, which modify the microstructure and, consequently, the material's hardness.

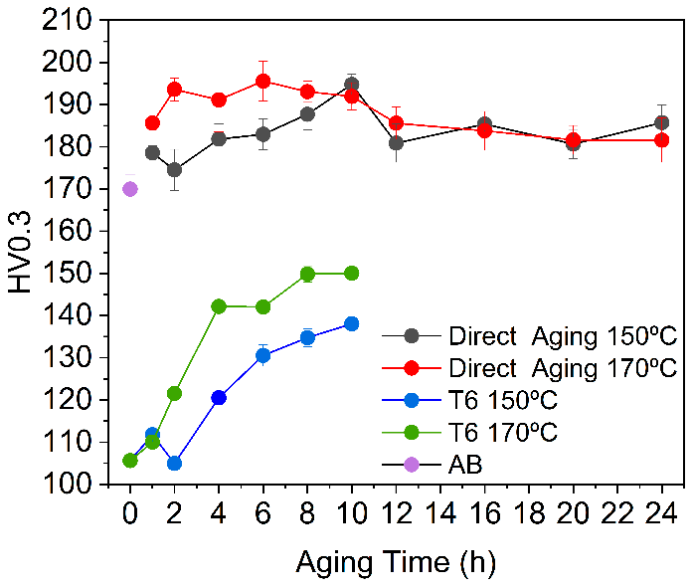

Figure 11. Aging curves of AlSi10Mg alloy obtained by L-PBF aged at 150 °C and 170 °C for different times, for direct aging and T6 heat treatment.

From Figure 11, the curve referring to the direct aging condition at 170 °C illustrates a rapid increase in hardness in the first hour of treatment, reaching the peak aging with a hardness of 195 HV in 6 h, which is an increase of 14.7% compared to the as-built condition (AB—purple dot in the image). In a comparative manner, although lower hardness values were achieved for the sample subjected to direct aging at 160 °C for 8 h—a result of the low hardness value obtained in the as-built condition (134 HV)—the hardness increase achieved by Zheng et al. [36] was on the order of 17%, which is equivalent to that found in the present experiment. After this peak, there is a drop followed by stabilization around 180 HV. In the direct aging condition at 150 °C, the hardness increase is more gradual, reaching levels like those of the previous condition, but in longer times (between 8 and 10 h). There is also a drop after the peak hardness, with subsequent stabilization around 180 HV.

On the other hand, the curves corresponding to the T6 treatment, both for the aging temperatures of 150 °C and 170 °C, have lower hardness values than the direct aging conditions. In the T6 condition at 150 °C, the hardness starts from 105 HV, corresponding to the T0 state (solubilized only), gradually increasing to 138 HV after 12 h of treatment. The T6 condition at 170 °C presents a similar behavior, but with higher values, reaching 150 HV. Such behavior was observed by Egidio et al. and Tang et al. [23,24]. After T6 treatment, the typical cell structures of the L-PBF process disappear, and the silicon particles coalesce, resulting in larger particles. The absence of the fine cellular network reduces barriers to dislocation movement and, consequently, the decrease in hardness and resistance, compared to the as-built state or with the direct aging treatment, which maintains finer and denser silicon particles [25].

Figure 12 presents the micrographs obtained by Scanning Electron Microscope of the samples in the (a) as-built state, (b) after direct aging at 170 °C for 6 h, and (c) after direct aging at 170 °C for 24 h, respectively.

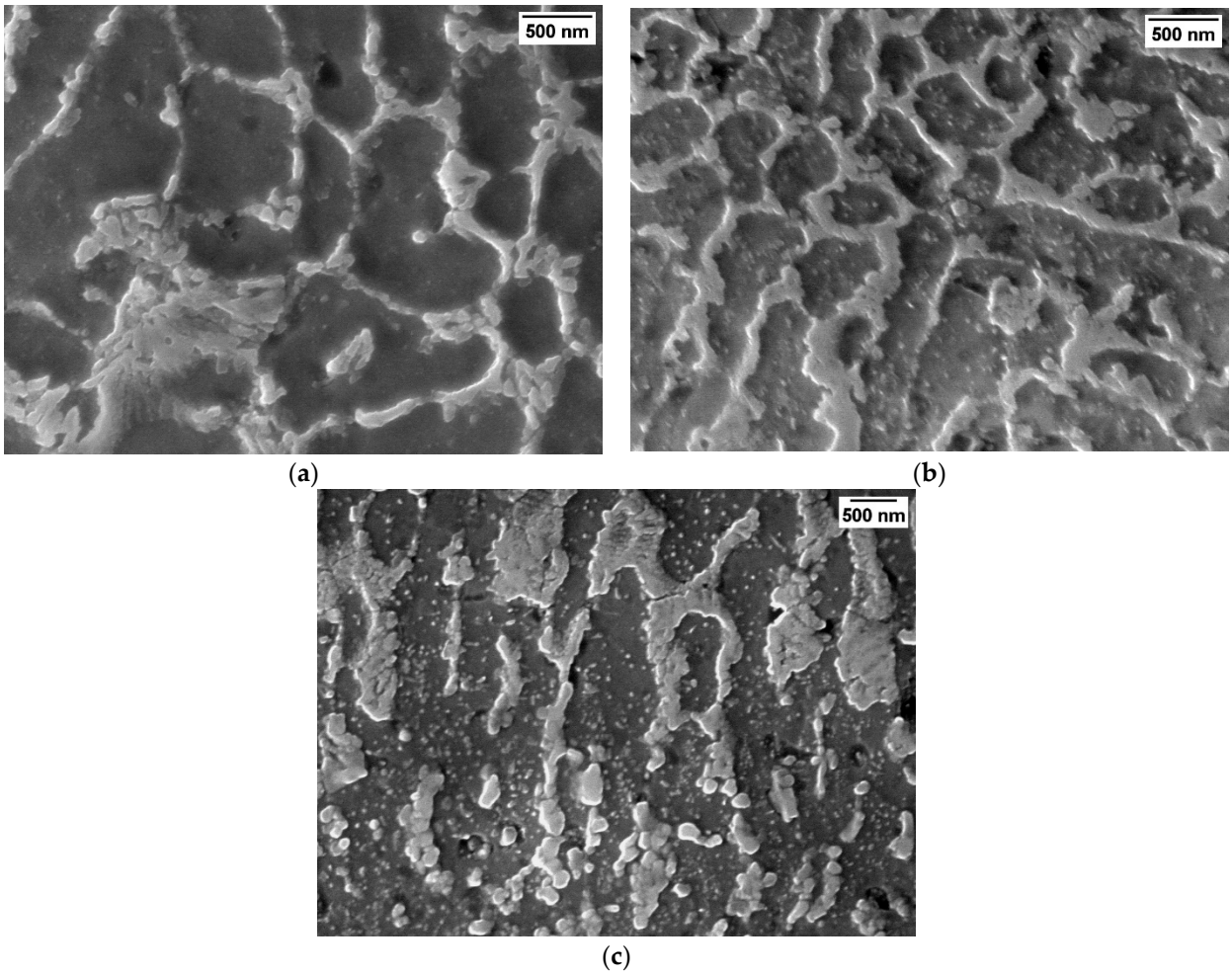

(**a**) (**b**)

(**c**)

Figure 12. Sample micrographs (**a**) as-built state. (**b**) Sample subjected to direct aging at 170 °C/6 h. (**c**) Sample subjected to direct aging at 170 °C/24 h.

The micrographs from Figure 12 illustrates that both the as-built sample and the sample subjected to direct aging at 170 °C for 6 h and 170 °C for 24 h exhibit a fine cell microstructure, typical of the L-PBF process, which involves high cooling coefficients. These cellular structures consist of a eutectic silicon network surrounding α-Al cells. These cells range in size from 1 to 4 μm.

In the as-built sample, nanoparticles are observed within the α-Al cells. These nanoparticles are rich in silicon and exhibit coherence with the aluminum matrix [24].

The direct aging heat treatment promoted precipitation and growth of nanosized silicon phases within cells while preserving overall cell structure and silicon network—behavior also reported by Baek et al. [25]. Comparing the microstructures as-built and direct aged at 170 °C/6 h, it is possible to observe a greater quantity of Si-rich nanoparticles within α-Al cells to aged microstructure. The precipitation process starts with the supersaturated solid solution α (SSS). As the intensity of thermal exposure increases (through higher temperatures or longer times), the hardening precipitates coalesce, passing through intermediate forms (β′ and β′), until they reach incoherent and stable phases of β, as evidenced by the aging curves. These larger precipitates contribute less to alloy hardening due to (i) a smaller interface area between the precipitates and the matrix; (ii) greater incoherence between the hardening phases and the α-Al matrix; and (iii) reduced density of dispersed particles [9].

In conditions with high temperatures and prolonged times, the silicon eutectic network may fragment at points of discontinuity, such as joints or junctions of the Si branches, due to the diffusion of the atoms. This results in a reduction in the hardness and, consequently, of the mechanical properties of the alloy—a phenomenon observed in the sample subjected to direct aging at 170 °C for 24 h, in which the breakdown of the eutectic silicon network and the presence of coalesced Si particles and Si nanoprecipitates can be identified [23].

Figure 13 shows the X-ray diffraction analyses of the heat-treated samples, the powder, and the as-built sample.

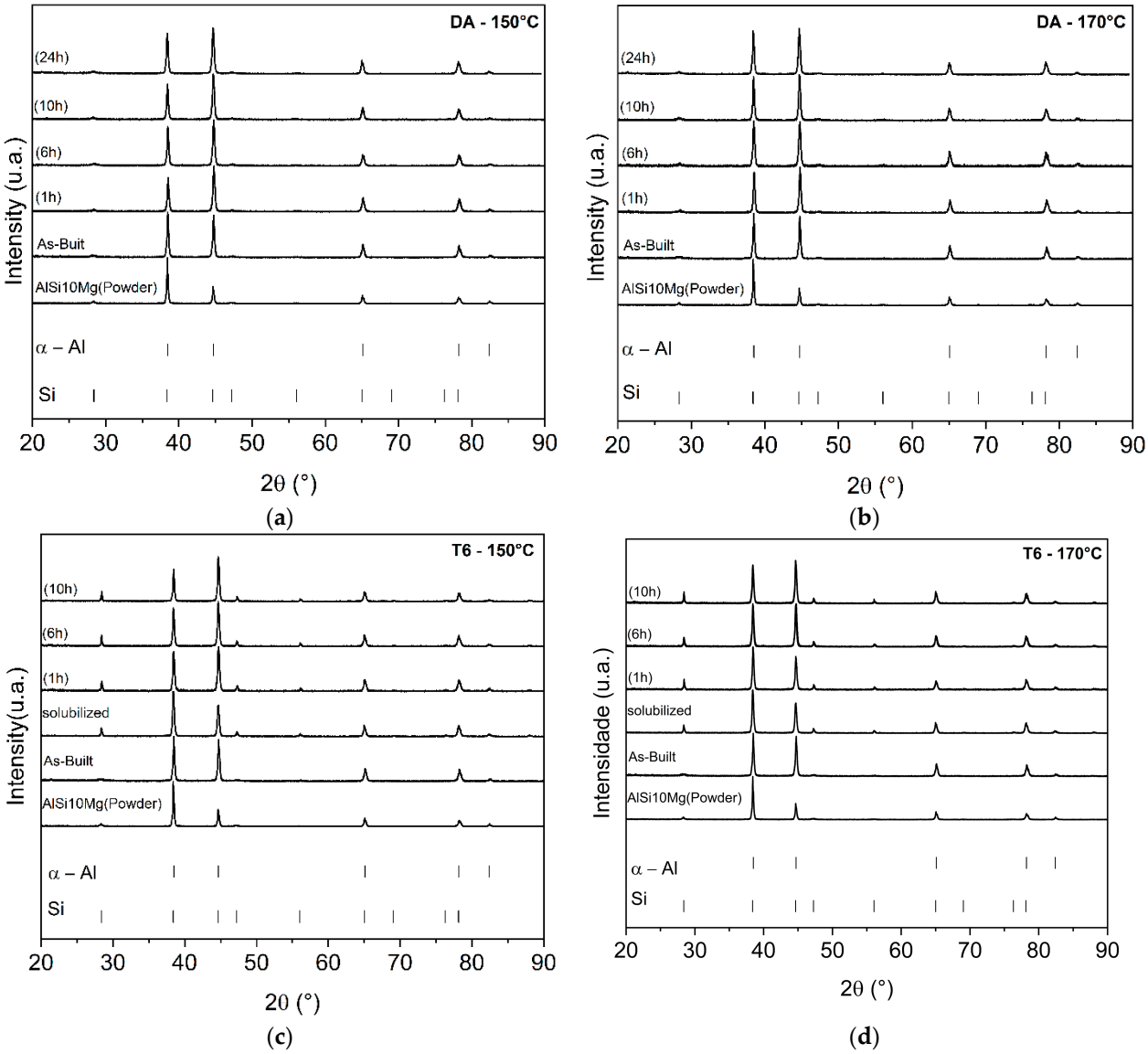

Figure 13. X-ray diffractograms (**a**,**b**) samples subjected to direct aging at 150 °C and 170 °C, respectively, and (**c**,**d**) samples subjected to T6 with aging at 150 °C and 170 °C, respectively, for different treatment times.

The presence of the α-Al and Si phases could be observed in all samples, mainly by the peak 28° in 2θ. In the samples submitted to direct aging and in the as-built condition, the widening of the peaks in the diffractograms indicates the presence of a fine cell microstructure, with nanometric precipitates dispersed in the α-Al cells, as evidenced by the micrographs presented in Figure 12. On the other hand, a higher crystallinity associated with the Si phase is evident in the samples submitted to the T6 treatment and can be ob-

served in X-ray diffractograms by the decrease in the width of the peaks related to Si. The narrowing of the peaks suggests the degradation of the eutectic structure and the growth of Si particles in size and quantity. This behavior can be attributed to the greater atomic mobility provided by the heat treatment conditions, which favors the diffusion of silicon from the supersaturated solid solution in the aluminum matrix. Therefore, precipitation, growth, and coalescence of Si particles occur—a behavior also observed by Tütük et al. [37].

3.4. Mechanical Tests

Figure 14 shows the stress–strain curves of the specimens in the as-built state and samples subjected to direct aging. For this treatment, the time conditions in which the highest hardness was achieved for both temperatures were chosen.

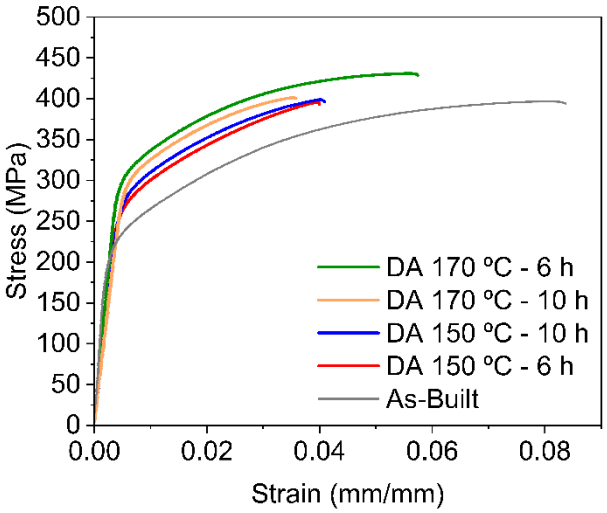

Figure 14. Stress–Strain curves of specimens treated by direct aging and as-built from AlSi10Mg Alloy obtained by L-PBF, and their mechanical properties.

From the stress–strain curves of the samples subjected to direct aging at 150 °C and 170 °C for 6 and 10 h, the curve referring to the as-built material and the obtained mechanical properties (Figure 14) shows that the modulus of elasticity is similar for all conditions, indicating that this property did not undergo significant changes with the heat treatment, as expected.

A variation in ultimate tensile strength was observed, increasing from 376.51 MPa in the as-built condition to 430.84 MPa in the sample subjected to direct aging at 170 °C for 6 h. This represents a 14.3% improvement in this property, close to the 14.7% increase in hardness. Zheng et al. [36] reported slightly lower ultimate tensile strength values for the as-built samples (356.7 MPa) and for the directly aged sample (396.5 MPa), although the hardness achieved for both conditions was also lower. This discrepancy between the literature and the present work may be attributed to several factors, such as differences in manufacturing parameters, which influence the size of the α-Al cells and the Si-eutectic network, variations in the Si nanoparticles size and concentration, and the presence of internal defects, all of which can affect the resulting properties. This result suggests that direct aging promoted optimized hardening, possibly related to the higher density of nanometric Si particles in α-Al cells, compared to the as-built state, as observed in the aging curves. These particles act as barriers to the dislocation movement, helping to increase mechanical strength. The lower tensile strength limit observed in the direct aging condition at 170 °C for 10 h may indicate an overaging process, characterized by the overgrowth of the precipitates, which reduces their effectiveness as a reinforcing mechanism. In addition, degradation of the Si eutectic network may occur, compromising the mechanical properties.

Evaluating and comparing the properties of the heat treatment conditions with the as-built condition elucidates that the heat treatments increased the tensile strength limit but decreased ductility. This exchange between strength and ductility is characteristic of heat treatments that aim to increase mechanical strength through precipitation, because by restricting the movement of disagreements, the material becomes more resistant, but less capable of accommodating significant plastic deformations [25].

4. Conclusions

In this study, in addition to the optimization of the manufacturing parameters of the AlSi10Mg alloy via powder bed fusion—mostly considering the 3D porosity and an evaluation of the distributions of diameters and sphericity of the pores—the effects of the T6 heat treatment (solution at 520 °C for 2h) and direct aging on the microstructure and mechanical properties of this alloy were investigated and compared, with aging at two temperatures for both treatments—150 °C and 170 °C—and varying aging times. The conclusions are as follows:

(1) In the optimization of the parameters in Step 1, the hatch space that provided the lowest volumetric porosity (0.29%) was 100 μm. Step 2 was designed to optimize power and scanning speed using the hatch space defined in the previous step. The best manufacturing conditions to minimize volumetric porosity (0.23%) were determined to be 300 W of power, a scanning speed of 800 mm/s, a layer thickness of 30 μm, and a beam diameter of 90 μm.

(2) The initial microstructure of the as-built samples had a fine cellular structure, typical of the L-PBF manufacturing process, composed of a network of α-Al cells surrounded by a eutectic silicon network, as well as silicon nanoparticles dispersed within the α-Al cells. The direct aging heat treatment preserved this microstructure, increasing the number of nanoparticles inside the cells. Furthermore, the silicon eutectic network fragmented under prolonged conditions, leading to the formation of coalesced particles and the breaking of the network, which compromises the mechanical strength of the material.

(3) The direct aging treatment at 170 °C, for 6 h, promoted the highest hardness, reaching a peak of approximately 195 HV, which represents an increase of about 14.7% over the as-built state. This result suggests that this procedure optimizes mechanical strength by promoting a microstructure with fine silicon particles. The T6 treatments, both at 150 °C and 170 °C, resulted in lower hardness values than those observed in direct aging, due to the loss of fine cell microstructure and the growth of silicon particles.

(4) For the direct aged samples, the tensile strength limit was significantly affected by the heat treatments, increasing by approximately 14.7% of the maximum value when passing from the as-built condition (376.51 MPa) to being aged at 170 °C for 6 h (430.84 MPa). In addition to the increased resistance, ductility was reduced in the samples submitted to direct aging, evidenced by the lower total elongation before the fracture. The direct aging condition at 170 °C for 6h offered the best balance between strength and ductility compared to the others studied, maintaining high strength without a pronounced decrease in deformation capacity.

Author Contributions: Conceptualization, G.d.L.X.R., A.A.C. and L.R.; methodology, G.d.L.X.R., R.d.O. and A.A.C.; software, G.d.L.X.R.; validation, L.R., M.M. and R.L.G.; formal analysis, G.d.L.X.R. and L.R.; investigation, R.d.O., L.R.; resources, A.A.C.; data curation, R.d.O., G.d.L.X.R. and M.M.; writing—original draft preparation, G.d.L.X.R.; writing—review and editing, A.A.C., L.R. and M.M.; supervision, A.A.C. and L.R.; project administration, A.A.C. and G.d.L.X.R.; funding acquisition, A.A.C. All authors have read and agreed to the published version of the manuscript.

Funding: The author Luís Reis also acknowledge Fundação para a Ciência e a Tecnologia (FCT) for its financial support via the project LAETA Base Funding (DOI: 10.54499/UIDB/50022/2020).

Data Availability Statement: The original findings of this study are fully presented in the article. For further information, please contact the corresponding author.

Acknowledgments: The authors are thankful for the funded by National Service for Industrial Apprenticeship (SENAI-SP/Brazil). The authors are thankful for the partial funding provided by the Mackenzie Research and Innovation Fund and the National Council for Scientific and Technological Development (CNPq-Brazil), under grant number 407050/2023-0. The authors also thank the Multiuser Analysis Center at IPEN for their support, and Arotec for performing the metallographic preparation using the Struers X-Matic equipment. The author Luís Reis also acknowledges Fundação para a Ciência e a Tecnologia (FCT) for its financial support via the project LAETA Base Funding (DOI: 10.54499/UIDB/50022/2020).

Conflicts of Interest: The authors declare no conflicts of interest.

Abbreviations

L-PBF	Laser powder bed fusion
DA	Direct aging heat treatment
T6	Solution + aging heat treatment

References

1. André, M.; Carlos, C.; Carlos, A.; Jonas, C.; Jorge, S.; José, F.; Milton, L.; Volpato, N. *Manufatura Aditiva—Tecnologias e Aplicações Da Impressão 3D*, 1st ed.; Editora Blucher: São Paulo, Brazil, 2017; ISBN 9788521211501.
2. Jawade, S.A.; Joshi, R.S.; Desai, S.B. Comparative Study of Mechanical Properties of Additively Manufactured Aluminum Alloy. *Mater. Today Proc.* **2020**, *46*, 9270–9274. [CrossRef]
3. Kotadia, H.R.; Gibbons, G.; Das, A.; Howes, P.D. A Review of Laser Powder Bed Fusion Additive Manufacturing of Aluminium Alloys: Microstructure and Properties. *Addit. Manuf.* **2021**, *46*, 102155. [CrossRef]
4. Gadlegaonkar, N.; Bansod, P.J.; Lakshmikanthan, A.; Bhole, K. A Review on Additively Manufactured AlSi10Mg Alloy: Mechanical, Tribological, and Microstructure Properties. *J. Mines Met. Fuels* **2025**, *73*, 87–101. [CrossRef]
5. Wang, P.; Rabori, A.S.; Dong, Q.; Ravkov, L.; Balogh, L.; Fallah, V. The Role of Cellular Structure, Non-Equilibrium Eutectic Phases and Precipitates on Quasi-Static Strengthening Mechanisms of as-Built AlSi10Mg Parts 3D Printed via Laser Powder Bed Fusion. *Mater. Charact.* **2023**, *198*, 112730. [CrossRef]
6. Gebhardt, U.; Gustmann, T.; Giebeler, L.; Hirsch, F.; Hufenbach, J.K.; Kästner, M. Additively Manufactured AlSi10Mg Lattices—Potential and Limits of Modelling as-Designed Structures. *Mater. Des.* **2022**, *220*, 110796. [CrossRef]
7. Fite, J.; Eswarappa Prameela, S.; Slotwinski, J.A.; Weihs, T.P. Evolution of the Microstructure and Mechanical Properties of Additively Manufactured AlSi10Mg during Room Temperature Holds and Low Temperature Aging. *Addit. Manuf.* **2020**, *36*, 101429. [CrossRef]
8. Eom, Y.S.; Park, J.M.; Choi, J.-W.; Seong, D.-J.; Joo, H.; Jo, Y.C.; Kim, K.T.; Yu, J.H.; Son, I. Fine-Tuning of Mechanical Properties of Additively Manufactured AlSi10Mg Alloys by Controlling the Microstructural Heterogeneity. *J. Alloys Compd.* **2023**, *956*, 170348. [CrossRef]
9. Zhang, X.; Chen, S.; Wang, Z.; Li, D.; Cui, X.; Xu, J. Effect of Cooling Rates and Heat Treatment Time on Si Phase of AlSi10Mg Alloy Manufactured by Selective Laser Melting: Microstructure Evolution and Strengthening Mechanism. *J. Alloys Compd.* **2024**, *1007*, 176494. [CrossRef]
10. Fiocchi, J.; Tuissi, A.; Biffi, C.A. Heat Treatment of Aluminium Alloys Produced by Laser Powder Bed Fusion: A Review. *Mater. Des.* **2021**, *204*, 109651. [CrossRef]
11. Guo, Q.; Zhao, C.; Qu, M.; Xiong, L.; Escano, L.I.; Hojjatzadeh, S.M.H.; Parab, N.D.; Fezzaa, K.; Everhart, W.; Sun, T.; et al. In-Situ Characterization and Quantification of Melt Pool Variation under Constant Input Energy Density in Laser Powder Bed Fusion Additive Manufacturing Process. *Addit. Manuf.* **2019**, *28*, 600–609. [CrossRef]
12. Poncelet, O.; Marteleur, M.; van der Rest, C.; Rigo, O.; Adrien, J.; Dancette, S.; Jacques, P.J.; Simar, A. Critical Assessment of the Impact of Process Parameters on Vertical Roughness and Hardness of Thin Walls of AlSi10Mg Processed by Laser Powder Bed Fusion. *Addit. Manuf.* **2021**, *38*, 101801. [CrossRef]
13. Gite, R.E.; Wakchaure, V.D. A Review on Process Parameters, Microstructure and Mechanical Properties of Additively Manufactured AlSi10Mg Alloy. *Mater. Today Proc.* **2023**, *72*, 966–986. [CrossRef]

14. King, W.E.; Barth, H.D.; Castillo, V.M.; Gallegos, G.F.; Gibbs, J.W.; Hahn, D.E.; Kamath, C.; Rubenchik, A.M. Observation of Keyhole-Mode Laser Melting in Laser Powder-Bed Fusion Additive Manufacturing. *J. Mater. Process Technol.* **2014**, *214*, 2915–2925. [CrossRef]
15. DebRoy, T.; Wei, H.L.; Zuback, J.S.; Mukherjee, T.; Elmer, J.W.; Milewski, J.O.; Beese, A.M.; Wilson-Heid, A.; De, A.; Zhang, W. Additive Manufacturing of Metallic Components—Process, Structure and Properties. *Prog. Mater. Sci.* **2018**, *92*, 112–224. [CrossRef]
16. Ferro, P.; Meneghello, R.; Savio, G.; Berto, F. A Modified Volumetric Energy Density-Based Approach for Porosity Assessment in Additive Manufacturing Process Design. *Int. J. Adv. Manuf. Technol.* **2020**, *110*, 1911–1921. [CrossRef]
17. Yadroitsev, I.; Krakhmalev, P.; Yadroitsava, I. Hierarchical Design Principles of Selective Laser Melting for High Quality Metallic Objects. *Addit. Manuf.* **2015**, *7*, 45–56. [CrossRef]
18. Larrosa, N.O.; Wang, W.; Read, N.; Loretto, M.H.; Evans, C.; Carr, J.; Tradowsky, U.; Attallah, M.M.; Withers, P.J. Linking Microstructure and Processing Defects to Mechanical Properties of Selectively Laser Melted AlSi10Mg Alloy. *Theor. Appl. Fract. Mech.* **2018**, *98*, 123–133. [CrossRef]
19. Hastie, J.C.; Kartal, M.E.; Carter, L.N.; Attallah, M.M.; Mulvihill, D.M. Classifying Shape of Internal Pores within AlSi10Mg Alloy Manufactured by Laser Powder Bed Fusion Using 3D X-ray Micro Computed Tomography: Influence of Processing Parameters and Heat Treatment. *Mater. Charact.* **2020**, *163*, 110225. [CrossRef]
20. Yang, T.; Liu, T.; Liao, W.; MacDonald, E.; Wei, H.; Zhang, C.; Chen, X.; Zhang, K. Laser Powder Bed Fusion of AlSi10Mg: Influence of Energy Intensities on Spatter and Porosity Evolution, Microstructure and Mechanical Properties. *J. Alloys Compd.* **2020**, *849*, 156300. [CrossRef]
21. Lehner, P.; Blinn, B.; Zhu, T.; Al-Zuhairi, A.; Smaga, M.; Teutsch, R.; Beck, T. Influence of the As-Built Surface and a T6 Heat Treatment on the Fatigue Behavior of Additively Manufactured AlSi10Mg. *Int. J. Fatigue* **2024**, *187*, 108479. [CrossRef]
22. Huang, N.; Luo, Q.; Bartles, D.L.; Simpson, T.W.; Beese, A.M. Effect of Heat Treatment on Microstructure and Mechanical Properties of AlSi10Mg Fabricated Using Laser Powder Bed Fusion. *Mater. Sci. Eng. A* **2024**, *895*, 146228. [CrossRef]
23. Di Egidio, G.; Tonelli, L.; Zanni, M.; Carosi, D.; Morri, A.; Ceschini, L. Direct Artificial Aging of the PBF-LB AlSi10Mg Alloy Designed to Enhance the Trade-off between Strength and Residual Stress Relief. *J. Alloys Metall. Syst.* **2024**, *5*, 100063. [CrossRef]
24. Tang, H.; Gao, C.; Zhang, Y.; Zhang, N.; Lei, C.; Bi, Y.; Tang, P.; Rao, J.H. Effects of Direct Aging Treatment on Microstructure, Mechanical Properties and Residual Stress of Selective Laser Melted AlSi10Mg Alloy. *J. Mater. Sci. Technol.* **2023**, *139*, 198–209. [CrossRef]
25. Baek, M.S.; Kreethi, R.; Park, T.H.; Sohn, Y.; Lee, K.A. Influence of Heat Treatment on the High-Cycle Fatigue Properties and Fatigue Damage Mechanism of Selective Laser Melted AlSi10Mg Alloy. *Mater. Sci. Eng. A* **2021**, *819*, 141486. [CrossRef]
26. Limbasiya, N.; Jain, A.; Soni, H.; Wankhede, V.; Krolczyk, G.; Sahlot, P. A Comprehensive Review on the Effect of Process Parameters and Post-Process Treatments on Microstructure and Mechanical Properties of Selective Laser Melting of AlSi10Mg. *J. Mater. Res. Technol.* **2022**, *21*, 1141–1176. [CrossRef]
27. Patel, S.; Chen, H.; Vlasea, M.; Zou, Y. The Influence of Beam Focus during Laser Powder Bed Fusion of a High Reflectivity Aluminium Alloy—AlSi10Mg. *Addit. Manuf.* **2022**, *59*, 103112. [CrossRef]
28. Yadroitsev, I.; Smurov, I. Surface Morphology in Selective Laser Melting of Metal Powders. *Phys. Procedia* **2011**, *12*, 264–270. [CrossRef]
29. Gibson, I.; Rosen, D.; Stucker, B.; Khorasani, M. *Additive Manufacturing Technologies*; Springer International Publishing: Cham, Switzerland, 2020; ISBN 9783030561277.
30. Herzog, D.; Seyda, V.; Wycisk, E.; Emmelmann, C. Additive Manufacturing of Metals. *Acta Mater.* **2016**, *117*, 371–392. [CrossRef]
31. King, W.E.; Anderson, A.T.; Ferencz, R.M.; Hodge, N.E.; Kamath, C.; Khairallah, S.A.; Rubenchik, A.M. Laser Powder Bed Fusion Additive Manufacturing of Metals; Physics, Computational, and Materials Challenges. *Appl. Phys. Rev.* **2015**, *2*, 041304. [CrossRef]
32. Gong, H.; Rafi, K.; Gu, H.; Starr, T.; Stucker, B. Analysis of Defect Generation in Ti-6Al-4V Parts Made Using Powder Bed Fusion Additive Manufacturing Processes. *Addit. Manuf.* **2014**, *1*, 87–98. [CrossRef]
33. Emminghaus, N.; Paul, J.; Hoff, C.; Hermsdorf, J.; Kaierle, S. Development of an Empirical Process Model for Adjusted Porosity in Laser-Based Powder Bed Fusion of Ti-6Al-4V. *Int. J. Adv. Manuf. Technol.* **2022**, *118*, 1239–1254. [CrossRef]
34. Kruth, J.P.; Levy, G.; Klocke, F.; Childs, T.H.C. Consolidation Phenomena in Laser and Powder-Bed Based Layered Manufacturing. *CIRP Ann. Manuf. Technol.* **2007**, *56*, 730–759. [CrossRef]
35. Fernandes, R.F.; Jesus, J.S.; Branco, R.; Borrego, L.P.; Costa, J.D.; Ferreira, J.A.M. Influence of Post-Processing Heat Treatment on the Cyclic Deformation Behaviour of AlSi10Mg Aluminium Alloy Subjected to Laser Powder Bed Fusion. *Int. J. Fatigue* **2022**, *164*, 107157. [CrossRef]

36. Zheng, Y.; Zhao, Z.; Xiong, R.; Ren, G.; Yao, M.; Liu, W.; Zang, L. Effect of Post Heat Treatment on Microstructure, Mechanical Property and Corrosion Behavior of AlSi10Mg Alloy Fabricated by Selective Laser Melting. *Prog. Nat. Sci. Mater. Int.* **2024**, *34*, 89–101. [CrossRef]
37. Tütük, İ.; Ural, M.M.; Yilmaz, M.S.; Özer, G. Development of an Alternative Heat Treatment to the Traditional T6 Heat Treatment of AlSi10Mg Alloy Produced by Additive Manufacturing. *J. Mater. Eng. Perform.* **2024**, *34*, 3112–3122. [CrossRef]